scientific reports

OPEN

Signatures of geostrophic turbulence in power spectra and third-order structure function of offshore wind speed fluctuations

So-Kumneth Sim[1], Joachim Peinke[2] & Philipp Maass[1✉]

We analyze offshore wind speeds with a time resolution of one second over a long period of 20 months for different heights above the sea level. Energy spectra extending over more than seven decades give a comprehensive picture of wind fluctuations, including intermittency effects at small length scales and synoptic weather phenomena at large scales. The spectra $S(f)$ show a scaling behavior consistent with three-dimensional turbulence at high frequencies f, followed by a regime at lower frequencies, where $fS(f)$ varies weakly. Lowering the frequency below a crossover frequency f_{2D}, a rapid rise of $fS(f)$ occurs. An analysis of the third-order structure function $D_3(\tau)$ of wind speed differences for a given time lag τ shows a rapid change from negative to positive values of $D_3(\tau)$ at $\tau \simeq 1/f_{2D}$. Remarkably, after applying Taylor's hypothesis locally, we find the third-order structure function to exhibit a behavior very similar to that obtained previously from aircraft measurements at much higher altitudes in the atmosphere. In particular, the third-order structure function grows linearly with the separation distance for negative D_3, and with the third power for positive D_3. This allows us to estimate energy and enstrophy dissipation rates for offshore wind. The crossover from negative to positive values occurs at about the same separation distance of 400 km as found from the aircraft measurements, suggesting that this length is independent of the altitude in the atmosphere.

Understanding offshore wind properties is a central problem for forecasting wind power and for estimating wind farm power outputs. Due to the turbulent nature of wind flows in the atmosphere, this is a challenging problem. For three-dimensional (3D) homogeneous isotropic turbulence, a description in terms of Kolmogorov's theory is possible. Its hallmark is a scaling of kinetic energy spectra with the wavenumber k according to a $k^{-5/3}$ law (K41 scaling)[1,2]. This scaling corresponds to a $f^{-5/3}$ scaling in the frequency domain when applying Taylor's hypothesis[3]. Atmospheric turbulence is, however, different because, apart from seasonal and diurnal influences, scaling features are affected by geometric constraints[4]. An improved understanding of its behavior is one of the grand challenges in wind energy science[5]. For offshore wind, where obstacles such as buildings, trees, and mountains are absent, one could ask whether a generic characterization of wind speed fluctuations over many orders of time or frequency scales is possible.

Spectra of horizontal wind speeds $v = (v_x^2 + v_y^2)^{1/2}$, with v_x and v_y being the components parallel to the Earth's surface, show a deviation from K41 scaling. When a measurement at a small height h in the boundary layer is performed, an isotropic and homogeneous inertial (IHI) range of 3D turbulence can no longer be assumed for length scales larger than h. In energy (power) spectra $S(f)$ of wind speeds, the corresponding crossover frequency $f_{IHI} \simeq \bar{v}_h/h$, with $\bar{v}_h$ the mean wind speed at height h, marks the onset of an intermediate regime $f_{2D} < f < f_{IHI}$ at lower frequencies, where $fS(f)$ varies weakly. This regime is sometimes referred to as the spectral-gap[6–8] and its features have been discussed controversially. There is evidence that its properties are dependent on the measurement height h[9,10]. Several studies suggest that the spectrum in this regime can show an f^{-1} scaling[11–14] and different models have been developed to explain such scaling[15–19]. Other fitting functions have been proposed also for describing the behavior[20,21].

For a long time, it has also been debated whether atmospheric turbulence is characterized by scaling properties of 2D turbulence[22–26]. For isotropic 2D turbulence, the seminal paper by Kraichnan[22] predicts a regime of f^{-3} scaling to occur at low frequencies as fingerprint of a forward enstrophy cascade, followed by an $f^{-5/3}$ scaling at even lower frequencies due to an inverse energy cascade. For geostrophic winds constrained by rotation and

[1]Fachbereich Physik, Universität Osnabrück, Barbarastraße 7, 49076 Osnabrück, Germany. [2]Institut für Physik & ForWind, Universität Oldenburg, Küpperweg 70, 26129 Oldenburg, Germany. ✉email: maass@uos.de

stratification[27,28], the theory by Charney[29] predicts that the potential enstrophy is the relevant conserved quantity analogous to 2D turbulence. Geostrophic turbulence behaves like 2D turbulence[29,30] because of its forward potential enstrophy cascade and conserved total energy[31,32]. The theory of quasi-2D geostrophic turbulence yields one regime of f^{-3} scaling in energy spectra. Nevertheless, energy spectra obtained from aircraft measurements show two scaling regimes with $f^{-5/3}$ and f^{-3} scaling. However, as pointed out by Lindborg[25], their appearance is not in agreement with the theoretical prediction for isotropic 2D turbulence, because the order of the regimes is reversed. This strongly suggests that the observed $f^{-5/3}$ scaling regime is not due to 2D turbulence. Stratified turbulence[33,34] and cascades of inertia gravity waves[27,35] are commonly discussed as possible explanations.

Here we show that spectra $S(f)$ of offshore wind speeds measured in the North Sea exhibit the commonly observed main features for frequencies $f > f_{2D}$ as discussed above. For $f < f_{2D}$, $S(f)$ rises strongly with decreasing f and shows a behavior consistent with the theoretical predictions for quasi-2D geostrophic turbulence in an interval around 10^{-5} Hz. This interval, however, is quite narrow and it is difficult to identify the f^{-3} scaling clearly.

By studying the wind speed fluctuation in the time domain, we provide further evidence that geostrophic turbulence dominates wind speed fluctuations for $f < f_{2D}$. This evidence comes from analyzing third-order structure functions $D_3(\tau)$, i.e. the third moment of differences between velocities separated by a time τ. The function $D_3(\tau)$ changes sign from negative[1] to positive values at time lags $\tau \simeq 1/f_{2D}$, where a positive $D_3(\tau)$ indicates a forward enstrophy cascade[32]. The zero-crossing of $D_3(\tau)$ at $1/f_{2D}$ is remarkably sharp. By revisiting spectra and third-order structure functions obtained from aircraft measurements[36,37], we find that frequencies or wavenumbers corresponding to r_{2D} agree with corresponding crossover frequencies to a f^{-3} scaling regime.

Data set and data analysis

Wind speeds were measured at the FINO1 platform in the North Sea, which is located about 45 km north from the island Borkum[38], see Fig. 1. They were sampled by three-cup anemometers over 20 months, from September 2015 to April 2017, for eight different heights h between 30 m and 100 m. The time resolution is $\Delta t = 1$ s,
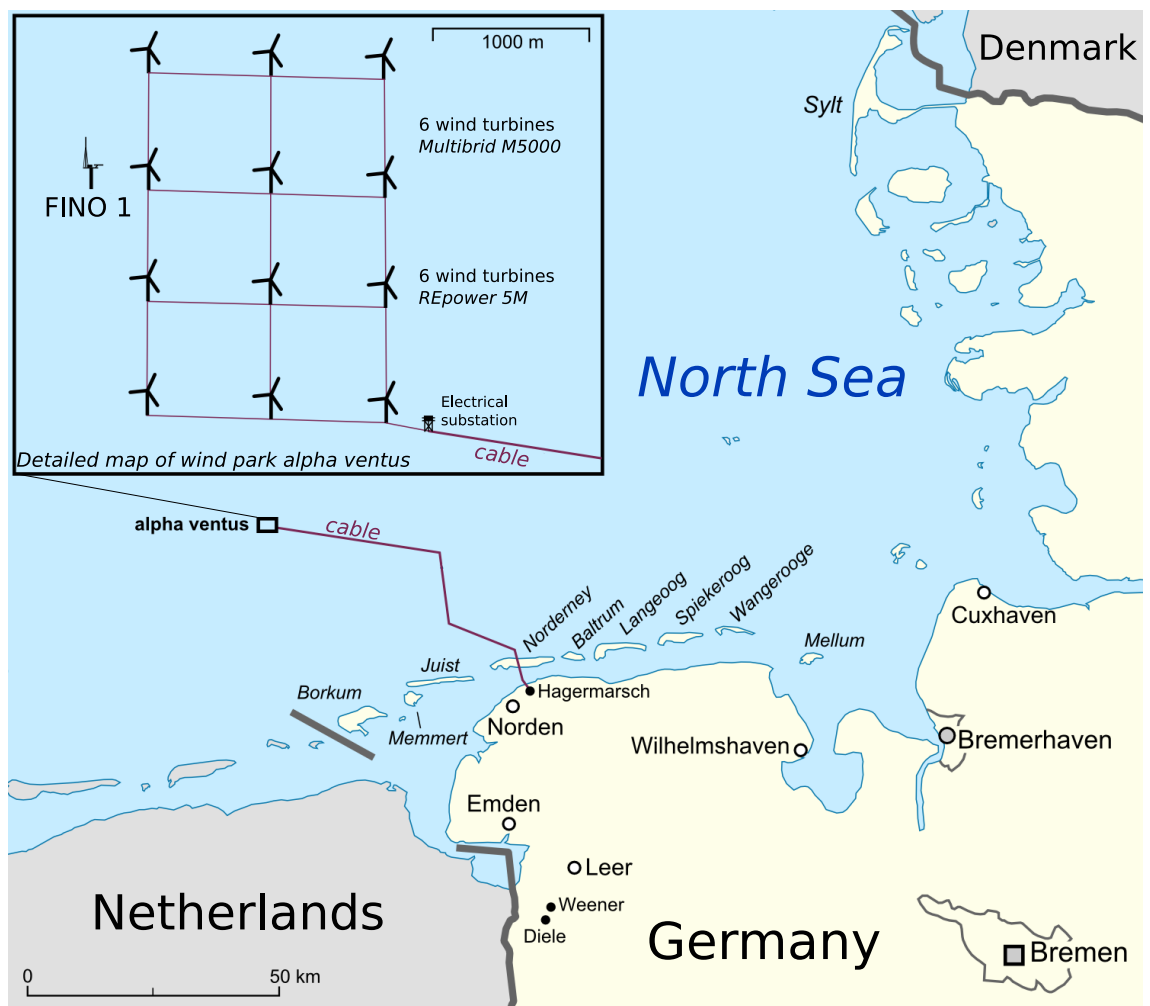

Figure 1. FINO1 platform, located at Alpha Ventus wind farm at Borkum West in the North Sea (54.3º N–6.5º W). Figure Wind park alpha ventus adapted from Lencer (CC BY-SA 3.0).

yielding time series with $N \cong 5 \times 10^7$ speed values for each height (for further details on the data sampling and instrumentation, see FINO - Database information).

The time series contain sequences of missing values of different lengths. These "not a number" (NaN) entries require special care in the data analysis, in particular when calculating energy spectra. Single missing values occur typically once a day, i.e. at about every 10^5th entry in the time series. A single NaN entry at a time t_{NaN} has been replaced by the interpolated value between the two wind speeds at the times $t_{\text{NaN}} \pm \Delta t$. In the resulting time series v_t of wind speeds, the fraction F_{NaN} of remaining NaN entries is given in Table 1. Time intervals with successive NaN entries are typically much longer than one second, indicating a temporary failure of the measurement device. The mean duration $\bar{T}_{\text{NaN}}$ of the respective intervals is 12 minutes for the measurement heights $h = 60\,\text{m}$ and $100\,\text{m}$, and almost one hour for $h = 30\,\text{m}$, see Table 1. How we handle these longer time intervals of successive NaN entries is explained below.

Diurnal variations of the offshore wind speeds did not show up as significant patterns in spectra or structure functions and we therefore did not apply a corresponding detrending of the data. We furthermore did neither consider seasonal variations nor changes of meteorologic stability[20], because we expect them to have only a weak effect on our principal results. Seasonal variations may affect our findings at very long times and corresponding low frequencies only.

Results of our analysis are presented for the three measurements heights $h = 30\,\text{m}, 60\,\text{m}$, and $100\,\text{m}$. The mean $\bar{v}_h$ and standard deviation σ_h of the wind speeds for these heights are listed in Table 1.

Energy spectra. For calculating energy spectra, we have used two methods to cope with longer periods of missing values.

In the first method, we determined spectra $S_\alpha(f)$ separately for all time intervals α with existing successive data. These spectra were averaged in bins equally spaced on the logarithmic frequency axis, yielding $S_{\text{ave}}(f)$.

Specifically, let $\{v_n\}_\alpha = \{v_n^{(\alpha)} \mid n = 0, \dots, N_\alpha - 1\}$ be the αth sequence of wind speeds without NaN values, $\alpha = 1, \dots, N_{\text{seq}}$, where N_{seq} is the number of these sequences. The discrete Fourier transform of $\{v_n\}_\alpha$ is

$$\hat{v}_m^{(\alpha)} = \sum_{n=0}^{N_\alpha - 1} v_n^{(\alpha)} e^{-2\pi i m n / N_\alpha}, \quad m = m_{\min}^{(\alpha)}, m_{\min}^{(\alpha)} + 1, \dots, m_{\max}^{(\alpha)}, \tag{1}$$

where $m_{\min}^{(\alpha)} = -\text{int}((N_\alpha - 1)/2)$ and $m_{\max}^{(\alpha)} = \text{int}(N_\alpha/2)$. The energy spectral density ("energy spectrum") of $\{v_t\}_\alpha$ at the frequency $f_m^{(\alpha)} = m/T_\alpha$ with $T_\alpha = N_\alpha \Delta t$ is

$$S_m^{(\alpha)} = S_{-m}^{(\alpha)} = \frac{2\Delta t^2}{T_\alpha} |\hat{v}_m^{(\alpha)}|^2, \quad m = 1, \dots, m_{\max}^{(\alpha)}. \tag{2}$$

These values $S_m^{(\alpha)}$ for frequencies $f_m^{(\alpha)}$ were averaged in ten bins every decade with equidistant spacing on a logarithmic frequency axis. The left and right border of the jth bin are denoted as f_j^- and f_j^+, respectively. The averaged energy spectrum in the jth bin is

$$\bar{S}_j = \frac{\sum_{\alpha=1}^{N_{\text{seq}}} \sum_{m=1}^{m_{\max}^{(\alpha)}} S_m^{(\alpha)} I_j(f_m^{(\alpha)})}{\sum_{\alpha=1}^{N_{\text{seq}}} \sum_{m=1}^{m_{\max}^{(\alpha)}} I_j(f_m^{(\alpha)})}, \tag{3}$$

where $I_j(.)$ is the indicator function of the jth bin interval $[f_j^-, f_j^+[$, i.e. $I_j(f) = 1$ for $f \in [f_j^-, f_j^+[$ and zero otherwise. The $\bar{S}_j$ value gives $S_{\text{ave}}(f)$ at the frequency $f = (f_j^- f_j^+)^{1/2}$,

$$S_{\text{ave}}(f_j) = \bar{S}_j. \tag{4}$$

In the second method, each interval of successive missing values was linearly interpolated between the two wind speed values terminating the interval. The resulting series covers the total time span of 20 months and we calculated its energy spectrum $S_{\text{tot}}(f)$. This spectrum should agree with $S_{\text{ave}}(f)$ for frequencies $f \lesssim 1/\bar{T}_{\text{NaN}}$ and perhaps higher frequencies. Indeed, as shown in Fig. 2 below, the spectra $S_{\text{tot}}(f)$ (full circles) agree with $S_{\text{ave}}(f)$ (open circles) in the intermediate frequency range $10^{-4}\,\text{Hz} \lesssim f \lesssim 10^{-2}\,\text{Hz}$, and even up to frequencies of $10^{-1}\,\text{Hz}$ (not shown). This demonstrates that $S_{\text{tot}}(f)$ is reliable for low frequencies $f < 1/\bar{T}_{\text{NaN}}$.

h	100 m	60 m	30 m
$\bar{v}_h\,[\text{ms}^{-1}]$	9.2	8.6	8.2
$\sigma_h\,[\text{ms}^{-1}]$	4.8	4.6	4.3
F_{NaN}	0.09%	0.09%	0.35%
$\bar{T}_{\text{NaN}}$	12 min	13 min	55 min

Table 1. Mean values $\bar{v}_h$ and standard deviations σ_h of offshore wind speeds for three measurement heights at the FINO1 platform in the North Sea. The number F_{NaN} gives the fraction of NaN entries in the time series that remain after having interpolated single NaN entries. The time $\bar{T}_{\text{NaN}}$ is the mean duration of intervals with successive NaN entries after single NaN interpolation.
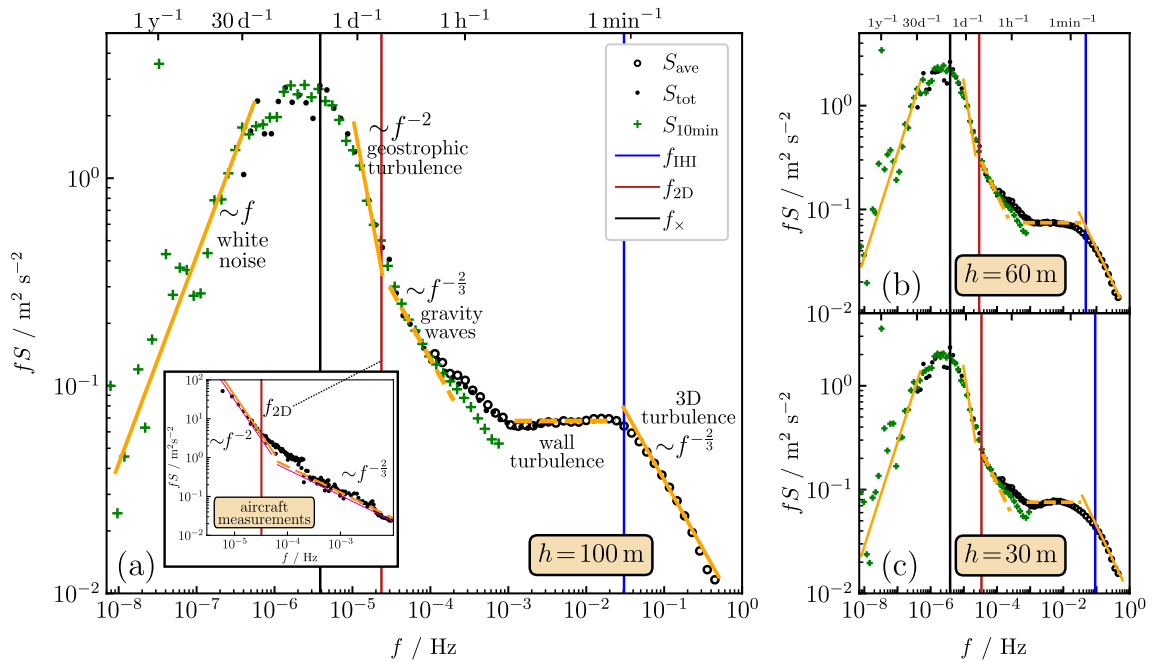
Figure 2. Frequency-weighted energy spectra in a double-logarithmic representation for three different heights (**a**) $h = 100$ m, (**b**) $h = 60$ m, and (**c**) $h = 30$ m. Open circles refer to $fS_{\text{ave}}(f)$, where $S_{\text{ave}}(f)$ is obtained by an averaging over all spectra of sub-sequences without missing values (see the description of the energy spectra calculation). Full circles refer to the total spectrum $S_{\text{tot}}(f)$, where linearly interpolated wind speeds were taken in all intervals of missing data. Green crosses mark spectra calculated from ten minutes averaged wind speeds in the period January 2005–July 2021. The vertical lines separate the various regimes: the blue line at frequency $f_{\text{IHI}} = \bar{v}_h/(3h)$ separates the scaling regime of 3D turbulence from the intermediate regime, the red line at frequency f_{2D} separates the intermediate regime from the regime of quasi-2D geostrophic turbulence, and the black line at frequency $f_{\times}$ marks the onset of uncorrelated wind speed fluctuations (white noise behavior). The theoretical scaling laws expected in the regimes of geostrophic and 3D turbulence are indicated by orange lines, as well as the white noise behavior at very low frequencies. The inset in (**a**) shows energy spectra obtained from aircraft measurements [extracted from Ref.[36] and mapped to the frequency domain by applying Taylor's hypothesis with a mean wind speed 30 ms^{-1}.].

Structure functions.

In the time domain, characteristic turbulence features can be identified in the scaling behavior of structure functions. The structure function $D_q(\tau)$ of qth order at time lag τ is the qth moment of the velocity fluctuation $[v_t - v_{t+\tau}]$,

$$D_q(\tau) = \left\langle [v_t - v_{t+\tau}]^q \right\rangle_t. \tag{5}$$

Here, $\langle \ldots \rangle_t$ means an average over all times. We determined the structure functions without replacing missing values by taking the average over all existing pairs $(v_t, v_{t+\tau})$. Knowing $D_q(\tau)$, one can transform this to a function $D_q(r)$ with $r = \bar{v}_h \tau$, where $\bar{v}_h$ is the mean wind speed averaged over the whole time series given in Table 1. This refers to applying Taylor's hypothesis "globally".

In a refined analysis, we take into account fluctuations of mean wind speeds on the scale τ. This corresponds to a method sometimes referred to as local Taylor's hypothesis. Specifically, for a given pair of times $t, t + \tau$ we first calculated the average wind speed $\bar{v}_{t,t+\tau}$ in the interval $[t, t+\tau[, \bar{v}_{t,t+\tau} = \sum_{\tau'=0}^{\tau-1} v_{t+\tau'}/\tau$. This gives a distance $r_{t,t+\tau} = \bar{v}_{t,t+\tau} \tau$ corresponding to Taylor's hypothesis, i.e. a pair of values $(r, \Delta v(r)) = (r_{t,t+\tau}, v_t - v_{t+\tau})$. The values $\Delta v(r)^q$ are subsequently averaged in fifty bins every decade with equidistant spacing on the logarithmic r axis, yielding $D_q^{\text{loc}}(r)$, where the superscript indicates the local use of Taylor's hypothesis. For comparison of $D_q^{\text{loc}}(r)$ with $D_q(\tau)$, we can transform $D_q^{\text{loc}}(r)$ back to a function depending on a time lag by using $D_q^{\text{loc}}(\tau) = D_q^{\text{loc}}(r/\bar{v}_h)$. Differently speaking, applying the local Taylor's hypothesis amounts to calculating the right-hand side of Eq. (5) for a transformed $\tau' = (\bar{v}_{t,t+\tau}/\bar{v}_h)\tau$.

In our analysis of the wind speed fluctuations in the time domain, we focus on the structure function $D_3(\tau)$ and the kurtosis given by

$$\kappa(\tau) = \frac{D_4(\tau)}{D_2(\tau)^2}. \tag{6}$$

When using Taylor's hypothesis locally, we insert $D_2^{\text{loc}}(\tau)$ and $D_4^{\text{loc}}(\tau)$ in this equation, yielding $\kappa^{\text{loc}}(\tau)$.

Results and discussion

Figure 2a shows the frequency-weighted energy spectrum fS vs. f for the measurement height $h = 100$ m in a double-logarithmic representation. When comparing the data in Fig. 2a with the corresponding frequency-weighted energy spectra for the other measurement heights in the range $h = 30 - 90$ m, we have found almost the same functional behavior. This is demonstrated in Fig. 2b and c, where we show the results for $h = 60$ m and 30 m. Similarly, the structure functions $D_q(\tau)$ in the time domain are nearly independent of h.

Figure 3a and c show the results for the third-order structure function for $h = 100$ m. We have plotted $D_3(\tau)^{1/3}$ in a semi-logarithmic representation to make changes of the function for small values easier visible. In Fig. 3a, $D_3(\tau)^{1/3}$ is displayed (indicated by "global"), and $D_3^{\text{loc}}(\tau)^{1/3}$ in Fig. 3c (indicated by "local"). The corresponding results for the kurtosis $\kappa(\tau)$ and $\kappa^{\text{loc}}(\tau)$ are shown in Fig. 3b and d. Overall, the results in Fig. 3a and b are similar to that of their counterparts in Fig. 3c and d, although there are differences in detail.

In the following, we first discuss our results for the energy spectra and structure functions in subsections referring to different frequency and respective time regimes. In a final subsection, we compare our findings for the third-order structure function in the crossover regime to quasi-2D geostrophic turbulence with literature results obtained from aircraft measurements.

IHI regime of 3D isotropic turbulence.   Above a frequency

$$f_{\text{IHI}} \sim \frac{\bar{v}_h}{h},\tag{7}$$

with $\bar{v}_h$ the mean wind speed [see Table 1], we see in Fig. 2a the signature of 3D turbulence, i.e., a behavior consistent with the K41 scaling. The border f_{IHI} of this frequency regime is marked by the vertical blue lines in the figure, and the K41 scaling behavior by the solid lines with slope $(-2/3)$.
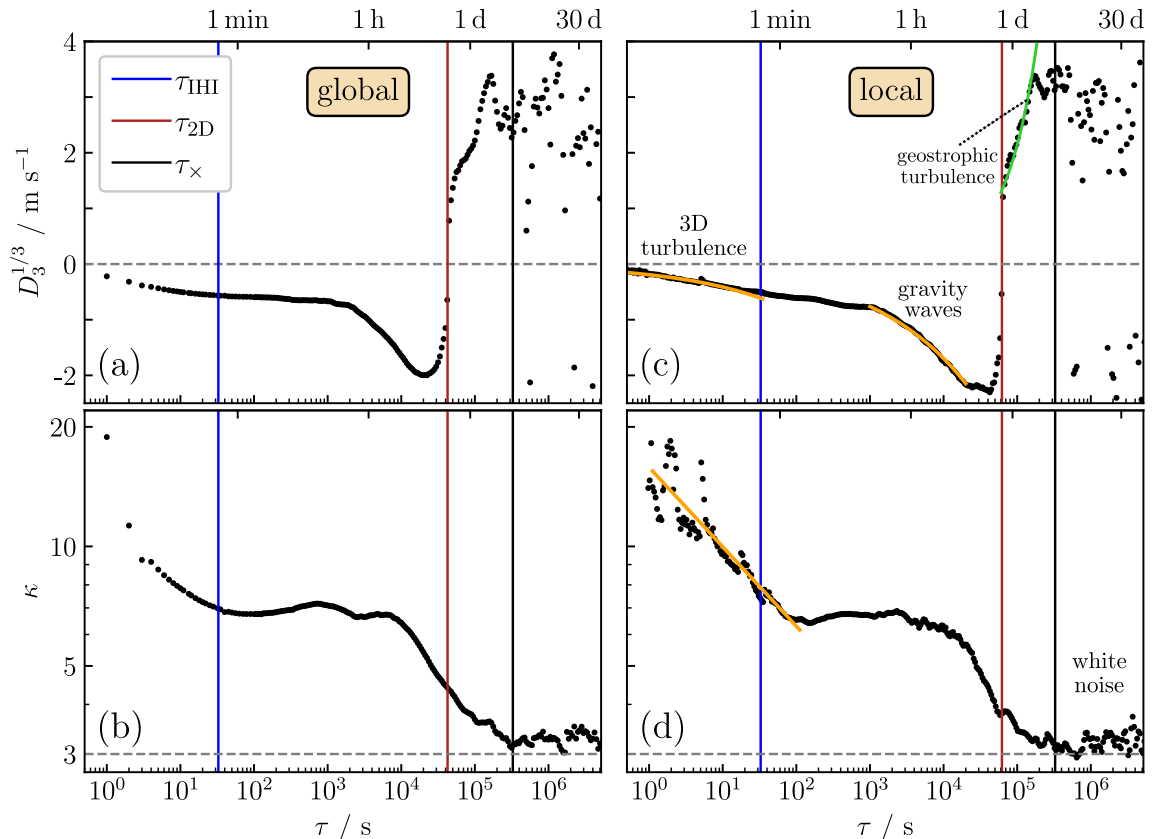

Figure 3. (**a**, **c**) Cubic root of the third-order structure function $D_3(\tau)$, and (**b**, **d**) kurtosis $\kappa(\tau)$ as a function of the time lag τ for the measurement height $h = 100$ m. Parts (**c**) and (**d**) show the results for $D_3^{\text{loc}}(\tau)^{1/3}$ and $\kappa^{\text{loc}}(\tau)$, when applying the local Taylor's hypothesis (see description of the data analysis). Vertical blue, red, and black lines correspond to the crossover frequencies in Fig. 2. In (**a**, **c**), the sharp change from negative to positive values at $\tau \gtrsim 1/f_{2D}$ indicates the transition to quasi-2D geostrophic turbulence. In (**c**), the orange line in the short-time (IHI) regime of 3D turbulence marks the function $-(4/5)\varepsilon_{\text{IHI}}\bar{v}_h\tau$ with $\varepsilon_{\text{IHI}} = 3 \times 10^{-3}$ m^{2}s^{-3} [cf. Eq. (8)], and the orange line in the regime of turbulence induced by gravity waves marks the function $-2\varepsilon\bar{v}_h\tau$ with $\varepsilon = 2.5 \times 10^{-5}$ m^{2}s^{-3} [cf. Eq. (10)]. In (**d**), the orange line with slope (-0.2) indicates corrections to K41 scaling corresponding to an intermittency factor $\mu = 0.45$. At large time lags $\tau > 1/f_\times$, $\kappa(\tau)$ is close to three, corresponding to a Gaussian distribution of velocity fluctuations.

For the structure functions, the theory of isotropic 3D turbulence[1] predicts a negative

$$D_3(r) = -\frac{4}{5}\varepsilon_{\text{IHI}}r,$$ (8)

where ε_{IHI} is the dissipation rate in the isotropic homogeneous inertial range. Taking into account the intermittency corrections to K41 scaling[39], the kurtosis should scale as

$$\kappa(\tau) \sim \tau^{-4\mu/9},$$ (9)

where μ is the intermittency factor and quantifies the amplitude of the logarithmic correction in the scaling of the energy dissipation rate with r. Values of μ lie in the range 0.2-0.5[40–42].

Both $D_3(\tau)$ and $D_3^{\text{loc}}(\tau)$ in Fig. 3a and c are negative in the regime $\tau \lesssim \tau_{\text{IHI}} = 1/f_{\text{IHI}}$. For the kurtosis shown in Fig. 3b and d, the time τ_{IHI} marks a crossover time from a regime where $\kappa(\tau)$ decreases to another regime where it is nearly constant. That $\kappa(\tau)$ is much larger than 3 for small τ reflects fat non-Gaussian tails in the distribution of wind speed fluctuations for short times[43].

As for the laws (8) and (9), the data in Fig. 3c and d can be well fitted to the respective equations, while this is not the case for the data in Fig. 3a and b. This shows that applying the local Taylor's hypothesis is needed here.

When fitting $-(4/5)\varepsilon_{\text{IHI}}\bar{v}_h\tau$ to the data for $D_3^{\text{loc}}(\tau)$ in Fig. 3b (orange line), we find $\varepsilon_{\text{IHI}} = 3 \times 10^{-3}\text{m}^2\text{s}^{-3}$ for the dissipation rate. This value compares well with results reported in other studies of turbulence in the atmospheric boundary layer[44]. When fitting Eq. (9) to the data for $\kappa^{\text{loc}}(\tau)$ in Fig. 3d (orange line), we obtain a slope corresponding to $\mu = 0.45$. Deviations from the respective line could be explained by the fact that cup anemometers loose precision for time lags approaching one second.

Intermediate regime of negative third-order structure function.

When f becomes smaller than f_{IHI}, Fig. 2a–c shows an intermediate regime (IR) where $fS(f)$ first varies weakly and the K41 scaling is absent. In this regime, the third-order structure function remains negative, see Fig. 3a and c.

On scales 10^{-3} Hz $\lesssim f < f_{\text{IHI}}$ in the IR, $fS(f)$ is almost constant, or, equivalently, $S(f) \sim f^{-1}$. Also, $D_3(\tau)$ and $\kappa(\tau)$ remain nearly constant in the corresponding time interval. We believe that this behavior reflects turbulent wind patterns strongly influenced by the Earth's surface, similarly as those found in wall turbulence experiments[45] for Reynolds numbers larger than 6×10^4 and in atmospheric boundary layers[11,14]. We therefore refer to the regime 10^{-3} Hz $\lesssim f < f_{\text{IHI}}$ as that of "wall turbulence", see Fig. 2a and denote the lower limit of this regime as f_{wt}, i.e. $f_{\text{wt}} \simeq 10^{-3}$ Hz. The scaling $S(f) \sim f^{-1}$ can be reasoned when considering wall turbulence to be governed by attached eddies[46]. Several models have been discussed to explain this scaling[15–19]. An f^{-1} scaling in the energy spectra corresponds to a logarithmic dependence of $D_2(\tau)$ on τ[47]. The second-order structure function follows this logarithmic behavior approximately for times $1/f_{\text{IHI}} \lesssim \tau \lesssim 10^3$ s (not shown), similarly as it has been found in near-surface atmospheric turbulence on land[48].

Below f_{wt} in the IR, $fS(f)$ increases with decreasing f. The structure function $D_3(\tau)$ in the corresponding time interval first decreases to larger negative values, and after passing a minimum rapidly rises towards zero. Interestingly, similar features have been seen in the analysis of wind speed data sampled by aircraft. Energy spectra obtained from aircraft measurements are shown in the inset of Fig. 2a. These data were extracted from Ref.[36] for different wavenumbers and mapped to the frequency domain by applying Taylor's hypothesis with a mean wind speed 30 ms^{-1} typical for the stratosphere. As will be discussed further below, the frequency range $f_{\text{2D}} < f < f_{\text{wt}}$ is likely connected to turbulent behavior induced by gravity waves.

Transition to quasi-2D geostrophic turbulence.

The IR regime terminates at a time lag τ_{2D}, above which $D_3(\tau)$ becomes positive, see Fig. 3a and c. We interpret f_{2D} as the frequency, below which quasi-2D geostrophic turbulence is governing wind speed fluctuations. According to the theory of geostrophic turbulence[29], a scaling $fS \sim f^{-2}$ is predicted due to a forward cascade of potential enstrophy[31], analogous to the enstrophy cascade of ideal isotropic 2D turbulence[22]. Indeed, Fig. 2a–c show a sudden rapid of fS increase towards lower f for $f \lesssim f_{\text{2D}}$. When f is close to f_{2D}, the data approach a line indicating the expected scaling law $fS \sim f^{-2}$. However, the spectral data alone do not provide convincing evidence for a transition to 2D turbulence. This is due to the limited extent of the frequency interval, where the data are consistent with the expected scaling behavior.

Strikingly, the transition becomes very well identifiable in Fig. 3a and c. Third-order structure functions of quasi-2D geostrophic turbulence[32] are similar to those of 2D turbulence, which are positive in general[49,50]. The third-order structure functions $D_3(\tau)$ in Fig. 3a and c indeed display a very sharp transition from negative to positive values at $\tau = \tau_{\text{2D}} \sim 1/f_{\text{2D}}$.

At the frequency $f = 1/\text{day}$ one could have expected a peak to occur due to diurnal variations. Such a peak has indeed been observed in the early analysis of onshore wind data by Van der Hoven[6]. A diurnal peak does not occur in Fig. 2a–c. We believe that this is because of weaker diurnal temperature variations of oceans compared to land masses. For identifying scaling laws of atmospheric turbulence, this is an advantage as well as the absence of mountains or other heterogeneities on land that can inject long-lived coherent structures.

3-day peak and white noise behavior at low frequencies.

For $\tau \gtrsim \tau_\times$, $\kappa(\tau)$ in Fig. 3b and d reaches a value $\kappa(\tau) \simeq 3$, reflecting Gaussian distributed wind speed fluctuations. The time $\tau_\times$ has a value of about 3 days and corresponds to a frequency $f_\times = 1/\tau_\times$, where $fS(f)$ in Fig. 2a–c runs through a peak maximum. This peak has been attributed to the motion of low and high pressure areas with linear dimension of about 10^3 km [6]. If we assume Taylor's hypothesis to hold even at large time scales of order $\tau_\times$, the corresponding spatial scale $r_\times = \bar{v}_h\tau_\times \simeq 3 \times 10^3$ km agrees with this length scale of low and high pressure areas.

For $r \gtrsim r_\times$, wind speed fluctuations can be expected to become uncorrelated. Accordingly, the energy spectrum should become constant for $f < f_\times$. To test this expectation, one needs very long time series to suppress numerical noise in the spectra. The FINO1 project[38] also provides ten minutes averaged wind speeds in the long period January 2005 until July 2021. Taking these data, we calculated energy spectra $S_{10min}(f)$ with the same method as used for obtaining S_{tot}. The results are represented by the green crosses in Fig. 2a–c and agree with S_{tot} and S_{ave} for frequencies below f_{2D}. In the low-frequency regime $f < f_\times$, they indeed show a behavior $fS_{10min} \sim f$ of a white noise spectrum. The particular high value of S_{10min} at the frequency of 1/year reflects the seasonal cycle of winds at the yearly time scale.

Comparison of third-order structure function at low altitude with results from aircraft measurements.

The third-order structure functions obtained from the wind speeds measured at low altitudes of ~ 100 m above the sea behave very similarly to those obtained from aircraft measurements at very high altitudes of ~ 10 km. For this comparison, we display our results for D_3 as a function of the distance r in Fig. 4a and b, where for transforming the time lags τ to distances r, we used in (a) the mean wind speed ($r = \bar{v}_h\tau$), and in (b) the local Taylor's hypothesis. The results from aircraft measurements were taken from Cho and Lindborg[37] and are redrawn in Fig. 4c. The third-order structure functions in Fig. 4a–c show the same overall behavior: a regime of negative D_3 at small $r_{2D} \lesssim \bar{v}_h\tau_{2D}$ (red symbols) is followed by a regime of positive values at large $r_{2D} \gtrsim \bar{v}_h\tau_{2D}$.

A merit of applying the local Taylor's hypothesis in our analysis becomes clear when comparing the data in Fig. 4a and b. While in Fig. 4b scaling regimes become visible, this is not the case in Fig. 4a. Notably, the results in Fig. 4b show a linear variation of D_3 with r in the regime of negative D_3, and an r^3-dependence in the regime of positive D_3, see the corresponding lines in the figure. These lines were obtained by least-square fits in the r intervals $10\,\text{km} < r < 200\,\text{km}$ and $600\,\text{km} < r < 1500\,\text{km}$.

It is insightful to compare the energy dissipation rate ε and the enstrophy flux η at the different altitudes, which can be extracted from the amplitude factors of the scaling laws. In the regime of linear variation of D_3 with r, the theory predicts, when incorporating Coriolis forces[51],

$$D_3 = -2\varepsilon r. \tag{10}$$

Our analysis yields $\varepsilon = 2.5 \times 10^{-5}\,\text{m}^2\text{s}^{-3}$, which is of similar magnitude as $\varepsilon = 6 \times 10^{-5}\,\text{m}^2\text{s}^{-3}$ obtained from the aircraft data[51]. For the forward enstrophy cascade, the theory predicts[25,32,51]

$$D_3(r) = \frac{1}{4}\eta r^3 \tag{11}$$

Our analysis gives $\eta = 6 \times 10^{-17}\,\text{s}^{-3}$, which is about 20 times smaller than the value $\eta \simeq 1.5 \times 10^{-15}\,\text{s}^{-3}$ reported for the aircraft measurements.

The length scale $r_{2D} \simeq 500$ km, where D_3 crosses zero, can be estimated. Geostrophic turbulence should arise when rotation and stratification constrain synoptic-scale winds to be nearly horizontal[27,28]. The length scale at which rotation becomes as important as stratification is described by the Rossby deformation radius with $r \simeq 500$ km as a standard estimation[34], which is the same as r_{2D}. A dimensional analysis[30,52,53] that requires only the enstrophy flux η and the energy dissipation rate ε yields a further estimation of r_{2D}. Assuming $\eta r_{2D}^3 \sim \varepsilon r_{2D}$, we find $r_{2D} \sim \sqrt{\varepsilon/\eta} \simeq 600$ km from the data in Fig. 4b, and $\sqrt{\varepsilon/\eta} \simeq 200$ km from the aircraft measurements in Fig. 4c. These estimates are of the same order of magnitude.

In the analysis of the aircraft measurements, the regime of linear variation $D_3(r) \sim r$ is related to a scaling regime $S \sim k^{-5/3}$ of corresponding wavenumbers k in kinetic energy spectra[54]. Gravity waves are commonly believed to be the physical mechanism leading to the corresponding scaling behaviors with the same functional form as for 3D isotropic turbulence[25,27,34,37,54]. We can ask whether the energy spectra for the wind speeds measured at low altitudes reflect this finding. The frequency interval corresponding to the r regime
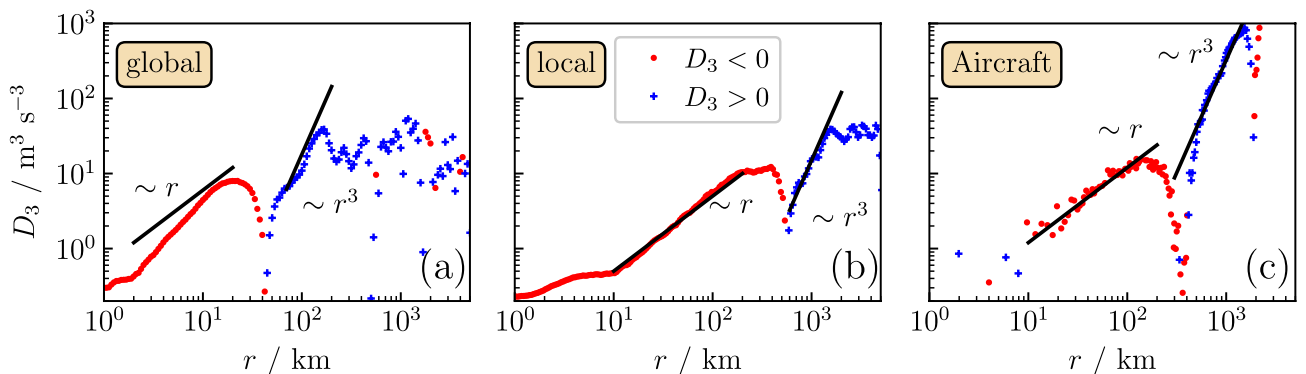

Figure 4. Third-order structure functions as function of separation distance r for low altitudes by applying Taylor's hypothesis with (**a**) a globally averaged velocity, (**b**) with local averages of velocities, and (**c**) for high altitudes taken from aircraft measurements. Blue crosses correspond to positive values of D_3 and red dots to negative ones. The theoretical scaling laws expected in the regimes of geostrophic and 3D turbulence are indicated by black lines.

$10 \, \mathrm{km} < r < 100 \, \mathrm{km}$ is $10^{-4} \, \mathrm{Hz} < f < 10^{-3} \, \mathrm{Hz}$. In this regime, the local slopes in the double-logarithmic plots in Fig. 2a–c indicate a behavior $fS \sim f^{-2/3}$ (or $S \sim f^{-5/3}$), shown by the orange dashed line in Fig. 2a.

Conclusions

Our analysis shows that the correlation behavior of offshore wind speed fluctuations at times between a few hours and several days is in agreement with the theory of quasi-2D geostrophic turbulence. While features of this turbulence were seen in previous studies based on aircraft measurements, we have found them here for low altitudes in offshore wind. The third-order structure function in the time domain shows a sharp transition from negative to positive values at a time τ_{2D}. Transforming the third-order structure function D_3 from the temporal to the spatial domain, it is strikingly similar to the aircraft data, if the local Taylor's hypothesis is used for the transformation. In that case, both the linear variation with the distance in a regime of negative D_3 (3D turbulence) and the cubic variation with the distance in a regime of positive D_3 (2D geostrophic turbulence) become visible. The transition between negative and positive D_3 occurs at about the same length scale 400 km for the offshore wind at a height 100 m and the wind measured by aircraft at a height of about 10 km. This strongly suggests that the length scale of the transition to 2D geostrophic turbulence is independent of the altitude.

We have given a comprehensive overview of the spectral behavior of offshore winds covering times from seconds to years. At low frequencies $f \ll f_\times \simeq 1/3$ days, a white noise behavior is found, i.e. correlations between wind velocities are not seen in the spectrum $S(f)$. Around $f_\times$, a peak appears in the frequency-weighted spectrum $fS(f)$ that can be explained by the motion of low- and high-pressure areas in the troposphere. For $f > f_\times$, the spectral energy decreases with increasing frequency. In a regime $f_\times < f < f_{2D} = 1/\tau_{2D}$, it decays as $S(f) \sim f^{-3}$ as predicted by the theory of geostrophic turbulence. For higher frequencies $f > f_{2D}$, results from aircraft measurements[36,54] show a weaker decay $S(f) \sim f^{-5/3}$, which has been interpreted as resulting from 3D turbulence induced by gravity waves. For the wind measured at a low altitude $h \sim 100$ m, we find indications of such a regime for f close to f_{2D}, but with increasing f the weighted spectrum $fS(f)$ soon becomes flat, before it enters for $f > f_{IHI}$ a regime of 3D isotropic turbulence. The crossover frequency f_{IHI} is about $\bar{v}/h$, where $\bar{v}$ is the mean wind speed. We believe that the intermediate regime $f_{2D} < f < f_{IHI}$ has two parts: one at high frequency due to wall turbulence with a behavior $S(f) \sim f^{-1}$, and a second one at higher frequencies, which is influenced by gravity waves. A scaling behavior according to gravity wave induced 3D turbulence, however, becomes clearly visible only at higher altitudes.

Our findings shed new light onto the characterization of wind speed fluctuations from micro- to synoptic scales and beyond. Frequencies of the order of f_{2D} correspond to mesoscale processes on length scales of 10-100 km. A better understanding of the relation between atmospheric phenomena on these mesoscales and microscales governing air flow around wind turbines and wind power plants, is considered as a grand challenge in wind energy science[5]. This in particular concerns multiscale approaches, where a detailed simulation on microscales has to be connected to coarse-grained approaches on large scales. We believe that our findings on geostrophic 2D turbulence below f_{2D}, the associated scaling of wind speed fluctuations, the indications of gravity-wave induced 3D turbulence close to f_{2D}, and the overall characterization of the different frequency regimes can improve the modeling of offshore wind flows across magnitudes of time scales.

Data availability

The wind velocity were measured at the FINO1 platform in the North Sea. The FINO1 project is supported by the German Government through BMWi and PTJ. The database is accessible via https://www.fino1.de/en.

References

1. Kolmogorov, A. N. Dissipation of energy in the locally isotropic turbulence. *Proc. R. Soc. London Ser. A* **434**, 15–17 (1991).
2. Hunt, J. C. R. & Vassilicos, J. C. Kolmogorov's contributions to the physical and geometrical understanding of small-scale turbulence and recent developments. *Proc. R. Soc. London Ser. A* **434**, 183–210 (1991).
3. Taylor, G. I. The spectrum of turbulence. *Proc. R. Soc. Lond. Ser. A* **164**, 476–490 (1938).
4. Wyngaard, J. C. *Turbulence in the Atmosphere* (Cambridge University Press, 2010).
5. Veers, P. *et al.* Grand challenges in the science of wind energy. *Science* **366**, eaau2027 (2019).
6. Van der Hoven, I. Power spectrum of horizontal wind speed in the frequency range from 0.0007 to 900 cycles per hour. *J. Atmos. Sci.* **14**, 160–164 (1957).
7. Fiedler, F. & Panofsky, H. A. Atmospheric scales and spectral gaps. *Bull. Am. Meteorol. Soc.* **51**, 1114–1120 (1970).
8. Metzger, M. & Holmes, H. Time scales in the unstable atmospheric surface layer. *Boundary-Layer Meteorol.* **126**, 29–50 (2008).
9. Larsén, X. G., Larsen, S. E. & Petersen, E. L. Full-scale spectrum of boundary-layer winds. *Boundary-Layer Meteorol.* **159**, 349–371 (2016).
10. Larsén, X. G., Petersen, E. L. & Larsen, S. E. Variation of boundary-layer wind spectra with height. *Q. J. R. Meteorolog. Soc.* **144**, 2054–2066 (2018).
11. Calaf, M., Hultmark, M., Oldroyd, H. J., Simeonov, V. & Parlange, M. B. Coherent structures and the k^{-1} spectral behaviour. *Phys. Fluids* **25**, 125107 (2013).
12. Fitton, G. *Multifractal analysis and simulation of wind energy fluctuations (Analyse multifractale et simulation des fluctuations de l'énergie éolienne).* Ph.D. thesis, schoolUniversité Paris-Est (2013).
13. Fitton, G., Tchiguirinskaia, I., Schertzer, D. & Lovejoy, S. Scaling of turbulence in the atmospheric surface-layer: Which anisotropy?. *J. Phys. Conf. Ser.* **318**, 072008 (2011).
14. Drobinski, P. *et al.* The structure of the near-neutral atmospheric surface layer. *J. Atmos. Sci.* **61**, 699–714 (2004).
15. Katul, G. G., Porporato, A. & Nikora, V. Existence of k^{-1} power-law scaling in the equilibrium regions of wall-bounded turbulence explained by Heisenberg's eddy viscosity. *Phys. Rev. E* **86**, 066311 (2012).
16. Nickels, T. B., Marusic, I., Hafez, S. & Chong, M. S. Evidence of the k_1^{-1} law in a high-Reynolds-number turbulent boundary layer. *Phys. Rev. Lett.* **95**, 074501 (2005).

17. Hunt, J. C. R. & Carlotti, P. Statistical structure at the wall of the high Reynolds number turbulent boundary layer. *Flow Turbul. Combust.* **66**, 453–475 (2001).
18. Nikora, V. Origin of the "−1" spectral law in wall-bounded turbulence. *Phys. Rev. Lett.* **83**, 734–736 (1999).
19. Korotkov, B. N. Kinds of local self-similarity of the velocity field of prewall turbulent flows. *Fluid Dyn.* **11**, 850–856 (1976).
20. Cheynet, E., Jakobsen, J. B. & Reuder, J. Velocity spectra and coherence estimates in the marine atmospheric boundary layer. *Boundary-Layer Meteorol.* **169**, 429–460 (2018).
21. Larsén, X. G., Larsen, S. E., Petersen, E. L. & Mikkelsen, T. K. Turbulence characteristics of wind-speed fluctuations in the presence of open cells: A case study. *Boundary-Layer Meteorol.* **171**, 191–212 (2019).
22. Kraichnan, R. H. Inertial ranges in two-dimensional turbulence. *Phys. Fluids* **10**, 1417–1423 (1967).
23. Gage, K. S. Evidence for a $k^{-5/3}$ law inertial range in mesoscale two-dimensional turbulence. *J. Atmos. Sci.* **36**, 1950–1954 (1979).
24. Lilly, D. K. Two-dimensional turbulence generated by energy sources at two scales. *J. Atmos. Sci.* **46**, 2026–2030 (1989).
25. Lindborg, E. Can the atmospheric kinetic energy spectrum be explained by two-dimensional turbulence?. *J. Fluid Mech.* **388**, 259–288 (1999).
26. Danilov, S. D. & Gurarie, D. Quasi-two-dimensional turbulence. *Phys. Usp.* **43**, 863 (2000).
27. Callies, J., Ferrari, R. & Bühler, O. Transition from geostrophic turbulence to inertia-gravity waves in the atmospheric energy spectrum. *PNAS* **111**, 17033–17038 (2014).
28. Oks, D., Mininni, P. D., Marino, R. & Pouquet, A. Inverse cascades and resonant triads in rotating and stratified turbulence. *Phys. of Fluids* **29**, 111109 (2017).
29. Charney, J. G. Geostrophic turbulence. *J. Atmos. Sci.* **28**, 1087–1095 (1971).
30. Vallgren, A., Deusebio, E. & Lindborg, E. Possible explanation of the atmospheric kinetic and potential energy spectra. *Phys. Rev. Lett.* **107**, 268501 (2011).
31. Vallgren, A. & Lindborg, E. Charney isotropy and equipartition in quasi-geostrophic turbulence. *J. Fluid Mech.* **656**, 448–457 (2010).
32. Lindborg, E. Third-order structure function relations for quasi-geostrophic turbulence. *J. Fluid Mech.* **572**, 255–260 (2007).
33. Lilly, D. K. Stratified turbulence and the mesoscale variability of the atmosphere. *J. Atmos. Sci.* **40**, 749 (1983).
34. Lindborg, E. The energy cascade in a strongly stratified fluid. *J. Fluid Mech.* **550**, 207–242 (2006).
35. Dewan, E. M. Stratospheric wave spectra resembling turbulence. *Science* **204**, 832–835 (1979).
36. Nastrom, G. D. & Gage, K. S. A first look at wavenumber spectra from gasp data. *Tellus A* **35A**, 383–388 (1983).
37. Cho, J. Y. N. & Lindborg, E. Horizontal velocity structure functions in the upper troposphere and lower stratosphere: 1. Observations. *J. Geophys. Res. Atmos.* **106**, 10223–10232 (2001).
38. FINO1 project supported by the German Government through BMWi and PTJ. The database is accessible via https://www.fino1.de/en.
39. Kolmogorov, A. N. A refinement of previous hypotheses concerning the local structure of turbulence in a viscous incompressible fluid at high Reynolds number. *J. Fluid Mech.* **13**, 82–85 (1962).
40. Sreenivasan, K. R., Antonia, R. A. & Danh, H. Q. Temperature dissipation fluctuations in a turbulent boundary layer. *Phys. Fluids* **20**, 1238–1249 (1977).
41. Arneodo, A. *et al.* Structure functions in turbulence, in various flow configurations, at Reynolds number between 30 and 5000, using extended self-similarity. *Europhys. Lett.* **34**, 411–416 (1996).
42. Vindel, J. M. & Yagüe, C. Intermitency of turbulence in the atmospheric boundary layer: Scaling exponents and stratification influence. *Boundary-Layer Meteorol.* **140**, 73–85 (2011).
43. Morales, A., Wächter, M. & Peinke, J. Characterization of wind turbulence by higher-order statistics. *Wind Energy* **15**, 391–406 (2012).
44. Muñoz-Esparza, D., Sharman, R. D. & Lundquist, J. K. Turbulence dissipation rate in the atmospheric boundary layer: Observations and WRF mesoscale modeling during the XPIA field campaign. *Mon. Weather Rev.* **146**, 351–371 (2018).
45. Chandran, D., Baidya, R., Monty, J. P. & Marusic, I. Two-dimensional energy spectra in high-Reynolds-number turbulent boundary layers. *J. Fluid Mech.* **826**, R1 (2017).
46. Perry, A. E. & Chong, M. S. On the mechanism of wall turbulence. *J. Fluid Mech.* **119**, 173–217 (1982).
47. Banerjee, T. & Katul, G. G. Logarithmic scaling in the longitudinal velocity variance explained by a spectral budget. *Phys. Fluids* **25**, 125106 (2013).
48. Ghannam, K., Katul, G. G., Bou-Zeid, E., Gerken, T. & Chamecki, M. Scaling and similarity of the anisotropic coherent eddies in near-surface atmospheric turbulence. *J. Atmos. Sci.* **75**, 943–964 (2018).
49. Cerbus, R. T. & Chakraborty, P. The third-order structure function in two dimensions: The Rashomon effect. *Phys. Fluids* **29**, 111110 (2017).
50. Xie, J.-H. & Bühler, O. Exact third-order structure functions for two-dimensional turbulence. *J. Fluid Mech.* **851**, 672–686 (2018).
51. Lindborg, E. & Cho, J. Y. N. Horizontal velocity structure functions in the upper troposphere and lower stratosphere: 2. Theoretical considerations. *J. Geophys. Res. Atmos.* **106**, 10233–10241 (2001).
52. Tung, K. K. & Orlando, W. W. The k^{-3} and $k^{-5/3}$ energy spectrum of atmospheric turbulence: Quasigeostrophic two-level model simulation. *J. Atmos. Sci.* **60**, 824–835 (2003).
53. Gkioulekas, E. & Tung, K.-K. Recent developments in understanding two-dimensional turbulence and the nastrom-gage spectrum. *J. Low Temp. Phys.* **145**, 25–57 (2006).
54. Nastrom, G. D., Gage, K. S. & Jasperson, W. H. Kinetic energy spectrum of large-and mesoscale atmospheric processes. *Nature* **310**, 36–38 (1984).

Acknowledgements

Author contributions

S.K.S. performed the data analyses. P.M. and J.P. supervised the work. All authors discussed and interpreted the results.

Funding

Competing interests

The authors declare no competing interests.

Additional information

Correspondence and requests for materials should be addressed to P.M.

Reprints and permissions information is available at www.nature.com/reprints.

Publisher's note Springer Nature remains neutral with regard to jurisdictional claims in published maps and institutional affiliations.